Journal of Materials Chemistry A

ROYAL SOCIETY OF CHEMISTRY

PAPER

View Article Online
View Journal | View Issue

Cite this: J. Mater. Chem. A, 2025, 13, 31569

Exploring hindered glymes as electrolyte solvents for sodium–oxygen batteries: impact on electrochemical performance and discharge product stability

Marina Enterría,[a] Sergio Rodriguez-Peña, †[ab] Idoia Ruiz de Larramendi, [b] Rosalia Cid, [a] Shanmukaraj Devaraj, [a] Javier Carrasco, [ac] Michel Armand [a] and Nagore Ortiz-Vitoriano *[ac]

Sodium–oxygen ($Na–O_2$) batteries are a promising alternative for high-energy storage applications, but their practical use is limited by electrolyte instability and poor cycling performance. This study investigates the role of hindered glymes—ether-based solvents with bulky *tert*-butyl groups—in improving the electrochemical behaviour of $Na–O_2$ batteries. We compare hindered glymes with conventional glymes in terms of discharge capacity, cycling stability, electrolyte interactions, and solid electrolyte interphase (SEI) composition. Although hindered glymes exhibit higher overpotentials, they outperform conventional glymes in cycle life. Post-mortem analysis confirms sodium superoxide (NaO_2) as the primary discharge product, but hindered glymes promote a greater formation of hydrated sodium peroxide, likely due to differences in the exposed surface area of discharge products. Molecular dynamics simulations reveal that steric hindrance in hindered glymes weakens Na^+–solvent interactions, facilitating Na^+ desolvation, which improves cycling stability. This steric effect also reduces Na^+ solvation, increases molecular rigidity, and limits discharge product stabilization, leading to higher polarization and smaller NaO_2 cubes during discharge. However, the improved Na^+ desolvation in hindered glymes enhances cycling performance, with hindered monoglyme (H-G1) showing a more pronounced effect due to its shorter chain. X-ray photoelectron spectroscopy (XPS) analysis demonstrates that weakened Na^+–solvent interactions lead to a more inorganic SEI, which contributes to improved interfacial stability. These results position hindered glymes as a promising electrolyte solution for $Na–O_2$ batteries, offering enhanced thermal and electrochemical stability while improving cycling performance.

Received 24th April 2025
Accepted 11th August 2025

DOI: 10.1039/d5ta03233d

rsc.li/materials-a

Introduction

Sodium–oxygen ($Na–O_2$) batteries have garnered significant interest as a promising alternative to conventional energy storage technologies due to their exceptionally high theoretical energy density, which has the potential to surpass that of lithium-ion batteries (LIBs).[1,2] This high energy density is primarily attributed to the conversion mechanism that occurs through the oxygen reduction reaction (ORR) during discharge and the oxygen evolution reaction (OER) during charge, where sodium reacts with oxygen to form solid discharge products such as sodium superoxide (NaO_2).[3,4] This mechanism enables a higher energy density compared to intercalation-based systems like LIBs. This makes $Na–O_2$ batteries particularly attractive for long-duration energy storage applications such as grid-scale renewable energy integration and electric transportation. However, despite their potential, the practical application of $Na–O_2$ batteries is currently hindered by several challenges, including low round-trip efficiency, high overpotentials, poor cycling stability and formation of undesirable discharge products during charge/discharge cycles. These issues are primarily attributed to the instability of the electrolyte, parasitic side reactions, and the formation of non-reversible discharge products, which compromise the performance and longevity of the batteries.[3,5–8]

The formation of solid discharge products plays a crucial role in determining the reversibility and overall efficiency of Na–

[a]Center for Cooperative Research on Alternative Energies (CIC energiGUNE), Basque Research and Technology Alliance (BRTA), Alava Technology Park, Albert Einstein 48, 01510 Vitoria-Gasteiz, Spain. E-mail: nortiz@cicenergigune.com

[b]Department of Organic and Inorganic Chemistry, Universidad del Pais Vasco (UPV/EHU), Barrio Sarriena s/n, 48940 Leioa, Spain

[c]Ikerbasque, Basque Foundation for Science, María Díaz de Haro 3, 48013 Bilbao, Spain

† Current address: Department of Energy Conversion and Storage, Technical University of Denmark, Fysikvej, 313, Kgs. Lyngby DK-2800, Denmark.

O_2 batteries. Ideally, sodium superoxide (NaO_2) should be the primary discharge product, as it offers low charge overpotentials and high rechargeability due to its easy decomposition back into Na and O_2.[9,10] However, the formation of NaO_2 is highly dependent on the electrolyte composition and solvation structure. The stability of superoxide intermediates (O_2^-) in solution largely determines whether NaO_2 forms in a controlled and reversible manner or if other more reactive species like sodium peroxide (Na_2O_2) or sodium oxide (Na_2O) form instead.[1] These alternative discharge products exhibit lower reversibility and higher parasitic reactivity, leading to electrode passivation, excessive polarization during charge, and reduced cycle life of the battery.

The selection of the electrolyte is therefore crucial for Na–O_2 battery performance as it influences discharge product formation, electrolyte stability, and interfacial reactions.[11,12] Among various electrolyte, ether-based solvents have emerged as prime candidates for Na–O_2 batteries due to their ability to coordinate with Na^+ ions through their oxygen donor atoms, forming stable solvation structures.[9] Glymes, a subset of ethers with the general formula $CH_3O[CH_2CH_2O]_nCH_3$, have been widely investigated due to their strong solvation properties, which directly influences the morphology and reversibility of discharge products.[11] Monoglyme (G1) and diglyme (G2) have demonstrated promising electrochemical performance, promoting the formation of cubic NaO_2 crystals with high reversibility, thereby reducing the energy required for battery recharge.[11]

Despite these advantages, conventional glymes face significant limitations, including safety concerns (*e.g.*, mutagenicity of the terminal O–CH_3 groups) and electrolyte instability (low flash points, susceptibility to oxidative degradation).[13,14] Recent studies have raised concerns regarding the mutagenic potential of traditional glymes with terminal O–CH_3 groups, suggesting that their long-term use in commercial applications may not be viable.[14,15] Furthermore, their relatively low flash points and susceptibility to oxidative degradation at high potentials pose additional risks related to flammability and electrolyte instability.[13] These limitations underscore the urgent need for safer and more sustainable electrolyte formulations for Na–O_2 batteries.

To address these limitations, recent research efforts have focused on modifying ether-based electrolytes to enhance their thermal stability, electrochemical robustness, and environmental safety.[14] We hypothesize that hindered glymes, a novel class of glymes where the terminal methoxy (–OCH_3) groups are replaced with bulkier *tert*-butyl ($C(CH_3)_3$) functional groups, could provide a promising solution for improving both the safety and performance of Na–O_2 batteries. The reasoning behind this hypothesis stems from the following key considerations: (i) increased molecular rigidity and reduced solvent flexibility: the introduction of bulky *tert*-butyl groups increases molecular rigidity and reduces solvent flexibility, which helps impede parasitic side reactions like solvent co-intercalation and oxidative degradation. This effect also facilitates more controlled Na^+ desolvation and the formation of stable discharge products like NaO_2, improving cycling stability; (ii) enhanced electrochemical stability: the steric hindrance of *tert*-butyl groups enhances the electrochemical stability by reducing oxidative degradation at high potentials, resulting in a more stable electrolyte and a longer operational lifespan; (iii) favourable solvation structure for Na^+: despite the steric hindrance, hindered glymes retain an effective Na^+ solvation structure, promoting reversible NaO_2 formation and minimizing the formation of side-products like Na_2CO_3 and $Na_2O_2 \cdot 2H_2O$, thus enhancing reversibility and reducing polarization during charge/discharge cycles; (iv) sustainable and safer electrolyte design: in addition to electrochemical benefits, the environmentally safer nature of hindered glymes—eliminating mutagenic O–CH_3 groups and enhancing thermal stability—makes them a sustainable alternative to conventional glymes, which are prone to volatility and degradation at high potentials.

Additionally, the use of sodium bis(trifluoromethylsulfonyl) imide salt (NaTFSI) and conventional glymes in Na–O_2 systems has traditionally been limited by poor cycling performance.[16] Our findings demonstrate that hindered glymes can enable the use of NaTFSI salts in Na–O_2 systems, improving electrolyte stability and providing a wider electrochemical window. NaTFSI also offers better stability at higher voltages, reducing the risks of decomposition and enhancing battery safety. Moreover, NaTFSI is chemically more stable in trace moisture, reducing corrosive side reactions compared to other common salts like $NaPF_6$, which can hydrolyse to form HF.

For the first time, we have shown that the combination of hindered glymes with NaTFSI salts provides a safer, more sustainable option for the development of high-performance Na–O_2 batteries, positioning hindered glymes as a promising electrolyte solvent for future Na–O_2 battery technologies. In this study, we present a systematic comparison between conventional glymes (G1 and G2) and their hindered counterparts containing *tert*-butyl functional groups (Fig. 1). We evaluate the impact of these hindered glymes on key electrochemical parameters, including discharge capacity, cycling stability, and interfacial reactions. Our study combines electrochemical characterization, spectroscopic analysis (including XPS and Raman spectroscopy), and computational modelling to explore how hindered glymes modify the solvation structure and Na^+–solvent interactions.

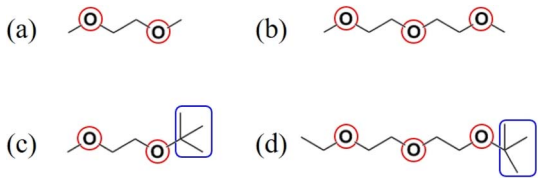

Fig. 1 Chemical structures of the four molecules analysed as solvents in this work: (a) 1,2-dimethoxyethane (G1, DME), (b) diethylene glycol dimethyl ether (G2, DEGDME), (c) ethylene glycol methyl-*tert*-butyl ether (H-G1), and (d) diethylene glycol ethyl-*tert*-butyl ether (H-G2). The oxygen atoms acting as charge-donating centres, which are the potential coordination sites for Na^+ cations, are highlighted in red, while the presence of the bulkier *tert*-butyl groups in hindered glymes is indicated in blue.

We demonstrate that hindered glymes improve cycling stability, reduce parasitic side reactions, and foster a more stable anode–electrolyte interphase compared to conventional glymes, albeit at the cost of slightly higher overpotentials. The enhanced stability and chemical robustness observed in the hindered glymes make them a promising electrolyte solution for Na–O_2 batteries, offering a safer and more sustainable alternative to conventional solvents. The novelty of this study lies in the comprehensive analysis of hindered glymes in Na–O_2 systems, providing new insights into electrolyte design for long-term stability and improved performance.

Experimental

Materials

Sodium bis(trifluoromethanesulfonyl)imide (NaTFSI, 99.5% purity) was purchased from Solvionic, and ethylene glycol dimethyl ether (G1, anhydrous, 99.5%) and diethylene glycol dimethyl ether (G2, anhydrous, 99.5%) were purchased from Sigma Aldrich. Ethylene glycol methyl-*tert*-butyl ether (H-G1) and diethylene glycol ethyl-*tert*-butyl ether (H-G2) were custom synthesized by Specific Polymers (France). The synthesis of these glymes involves an acid-catalysed addition of isobutene to the OH group of $RO(C_2H_4O)_nC_2H_4OH$ (*tert*-G1: R = CH_3, $n = 0$; *tert*-G2: R = C_2H_5, $n = 1$). Prior to use the glymes were distilled using bulb to bulb distillation technique over NaH in a Buchi-B585.[13] All the glymes were dried over molecular sieves (3 Å, Sigma Aldrich) for two weeks prior to their use. NaTFSI was dried under vacuum at 120 °C for 48 h. The electrolyte was prepared by mixing 0.5 M NaTFSI and the corresponding solvent in the glovebox. The selected electrolyte concentration demonstrated the best battery performance in prior studies conducted by our group.[12] The water content in all the prepared electrolytes was determined by an 899 Karl Fischer coulometer (Metrohm) and was below 10 ppm. A gas diffusion layer – GDL – (Quintech, Freudenberg H23C6) was used as air cathode, which was dried under vacuum at 100 °C overnight. Afterwards, it was stored in the Ar-filled glove box without exposure to air.

Cell assembly and electrochemical measurements

In this work, 2-electrode Swagelok®-type cells equipped with an oxygen reservoir were used for evaluating the electrochemical performance of different glymes as solvents on the electrolyte formulation. Celgard® H2010 membrane soaked in 200 μL of electrolyte was used as the separator and a sodium metal disc (Panreac, 99.8% purity) as both the reference and counter electrode. All the materials were dried and transferred to an argon glovebox prior to their manipulation. The assembled cells were filled with pure oxygen (99.99% pure) to around 1 atm and rested for 8 h at open circuit voltage (≈2.2–2.3 V *vs.* Na^+/Na) before the electrochemical measurements. Galvanostatic deep-discharge measurements were performed in a Biologic-SAS VMP3 potentiostat at 75 μA cm^{-2} setting a lower cut-off voltage of 1.8 V *vs.* Na^+/Na. Shallow cycling measurements by galvanostatic charge/discharge were performed at a current of 75 μA cm^{-2} to a capacity limitation of 0.25 mAh cm^{-2} with a potential cut-off between 1.8 and 3.2 V *vs.* Na^+/Na.

The impedance evolution during ten cycles was analyzed using the same voltage window, current and capacity limitation. Electrochemical impedance spectroscopy (EIS) was performed every two hours during the first cycle, and subsequently at the end of discharge and charge in each of the following nine cycles. This test was conducted on the same potentiostat using 3-electrode cells with a piece of metallic sodium as the reference electrode. EIS spectra were recorded over a frequency range of 1 MHz to 10 mHz, using an AC signal amplitude of 10 mV and 0.1 point per decade. Impedance spectra were analysed using Scribner Associates' ZView software.

Physicochemical characterization of pristine and discharged electrodes

Morphological characterization of the discharged and cycled electrodes was conducted by scanning electron microscopy (SEM) imaging using a FEI Quanta 250 microscope operated at 20 kV. The electrodes were transferred from an Ar-filled glove box to the SEM using an air-tight holder to avoid air exposure. Raman spectra were recorded, with a Renishaw inVia confocal Raman spectrometer (serial number 16H981) at room temperature (20 °C), to examine the nature of the discharge products. The incident laser applied in this work has a wavelength of 532 nm, which was focused through an inverted microscope, *via* a 50× objective lens (Leica). The spectra were recorder under 1% laser power by performing 10 acquisitions with 10 s of exposure time of the laser beam to the sample. A mapping of four points on the surface of each discharged electrode was performed to obtain a more representative analysis of the distribution and composition of the discharge products across various regions of the electrode surface. The nature of the battery discharge products was studied by powder X-ray diffraction (XRD) using a Bruker D8 Discover diffractometer with $\theta/2\theta$ Bragg–Brentano geometry (monochromatic Cu radiation: Kα1 = 1.54056 Å) within the 30–60° range (2θ), using a step size of 0.02°. The discharged and cycled electrodes were placed in an O-ring holder and a Kapton foil (7.5 microns) to isolate the sample, employing a silicon wafer as support. Two diffraction patterns were acquired at 30 min and 1 h to monitor the eventual degradation of the sample during the measurement.

Surface chemical analysis of cycled anodes

The chemical composition of the Solid Electrolyte Interphase (SEI) formed on the Na metal anodes was analyzed by X-ray Photoelectron Spectroscopy (XPS) using a Phoibos 150 XPS spectrometer (SPECS Surface Nano Analysis) installed in an UHV chamber with a base pressure of 5×10^{-10} mbar. The electrodes were transferred from the glovebox to the XPS chamber using an air-tight Ar-filled transfer tool. Spectra were collected in fixed analyzer transmission mode with a 2 mm lateral view on the sample. A non-monochromatic twin anode X-ray source (Mg Kα with $h\nu$ = 1253.6 eV and Al Kα with $h\nu$ = 1486.6 eV) was employed to produce the photoelectrons. Al anode was mainly used, except for measuring O 1s, in which case Mg anode was selected to avoid the overlapping signal of the Na KLL line. High resolution spectra were measured with

E_{step} = 0.1 eV and E_{pass} = 30 eV. The binding energy scale was calibrated by setting the aliphatic C–C bond at 284.8 eV. The inelastically scattered photoelectrons background was simulated by a Shirley function and Voigt profiles were selected as line shapes. Quantification of atomic surface species was done by using tabulated Scofield cross sections for the photoelectrons production. Several corrections were applied, such as the energy dependent analyzer transmission and variations in effective attenuation length (EAL) of the collected photoelectrons with different kinetic energies.

Computational study

Classical molecular dynamics (MD) simulations were performed over the system NaTFSI dissolved in 4 different glyme solvents (G1, G2, H-G1, H-G2) using GROMACS.[17,18] Each system was built by inserting 30 NaTFSI molecules in a simulation box, and the number of solvent molecules was set by performing previous simulation tests with each different solvent to match the NaTFSI concentration of 1 M once the system is optimized. The number of solvent molecules used were 255, 190, 175, and 125 for G1, G2, H-G1, and H-G2, respectively. All the molecules were placed randomly in an initial low-density box. Then the simulation box was compressed at 10 K and 10 atm applying the Berendsen thermostat and the Parrinello–Rahman barostat, respectively, with a relaxation time of 1.0 ps. After this, the system was gradually heated up to the simulation temperature of 298 K (25 °C) with a constant pressure of 1 atm to ensure proper dissolution of the salt, using a relaxation time of 20 ps for both Berendsen thermostat and Parrinello–Rahman barostat. The system was further equilibrated in a *NVT* ensemble at 298 K during 1 ns prior to the simulation run, which was set up at these same conditions for 50 ns to guarantee reaching a diffusive regime. Each system has been simulated 3 times, starting from different random configurations, to average the results and obtain better statistics.

The parameters of the force field for the Na^+, $TFSI^-$, G1, G2, H-G1, and H-G2 molecules were obtained using the OPLS-AA force field. The partial charges assigned to the solvent molecules were the predefined ones provided by the OPLS-AA force field.[19–24] However, in the case of the $TFSI^-$, its structure was optimized using density functional theory (DFT) calculations as implemented in the Fritz-Haber Institute *ab initio* molecular simulations (FHI-aims) software,[25,26] using the Becke three parameter Lee–Yang–Parr (B3LYP) functional,[27,28] together with the tight "tier 2" basis set predefined by FHI-aims. The atomic partial charges were computed using the electrostatic potential (ESP) method with a total charge of −1. To account for the polarizability effects, a scale factor of 0.7 was applied to the partial charges uniformly to all atoms. To keep the system neutrally charged, the partial charge of Na^+ was set to +0.7.

Results and discussion

The ionic conductivity of the electrolytes in this study is shown in Table 1. The hindered glymes H-G1 and H-G2 exhibit ionic conductivities of 2.46 and 1.05 mS cm^{-1}, respectively, while the unhindered glymes show values of 12.1 and 9.03 mS cm^{-1} for G1 and G2, respectively. These values are consistent with those reported for similar systems.[29] The higher ionic conductivity observed for the unhindered glymes relative to their hindered counterparts is consistent, as the incorporation of bulky tertiary end groups in the latter increases the viscosity of the solvents. Furthermore, the decreasing trend in ionic conductivity from monoglymes to diglymes—both hindered and unhindered—is attributed to the presence of two ethylene oxide units in diglymes, as opposed to a single ethylene bridge in monoglymes, which further contributes to the increased solvent viscosity.

Table 1 Ionic conductivity (mS cm^{-1}) measured for the electrolytes understudy

G1	G2	H-G1	H-G2
12.1	9.03	2.46	1.05

The full discharge capacity of Na–O_2 batteries incorporating different electrolyte formulations was investigated (Fig. 2). The discharge capacity for unhindered glymes and hindered monoglyme was quite similar, with 2.93 mAh cm^{-2} for G1, 2.82 mAh cm^{-2} for H-G1 and 2.7 mAh cm^{-2} for G2. H-G2 exhibited slightly lower discharge capacity, delivering 2.3 mAh cm^{-2}. These findings indicate that the chain length or the existence of bulkier substituent in the lineal alkyl chain of the solvent does not have a significant impact on the capacity. However, it does affect the discharge overpotential, with hindered glymes exhibiting markedly higher overpotentials. The glymes G1 and G2 exhibit lower overpotentials compared to the hindered glymes, with shorter-chain hinder glyme (H-G1) showing lower overpotential than its longer-chain counterparts (H-G2). This suggests that diglyme-based systems require more energy to produce the reaction products, which is also associated with

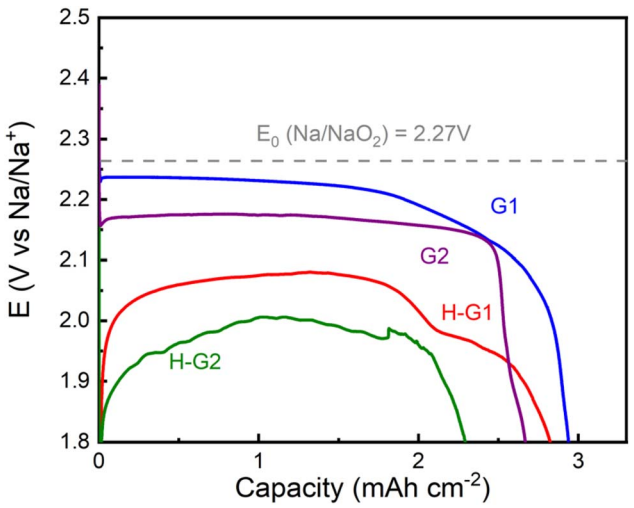

Fig. 2 Galvanostatic deep-discharge curves for sodium–oxygen batteries using different glymes as electrolytes at a current density of 75 μA cm^{-2} in 1 M NaTFSI. The grey dashed line indicates the standard reduction potential for the formation of sodium superoxide (NaO_2) from metallic sodium.

greater energy losses during the process. The presence of bulky *tert*-butyl groups appears to impose additional resistance to ion transport, necessitating a higher energy to overcome reaction barriers. In solvation chemistry, a contact ion pair occurs when a cation (Na^+) and its counteranion (O_2^-) are closely associated and interact strongly. In this state, the contact ion pair is typically solvated, meaning the solvent molecules surround the ions but the cation and anion still stay in proximity, without being fully dissociated. In contrast, separated ion pair refers to a situation where the cation and anion are no longer in close contact with each other. In this case, the ions are dissociated. The ions are individually solvated by the solvent, with the solvent molecules acting as a medium that prevents the cation and anion from recombining. In Na–O_2 batteries, separated ion pairs are typically preferred because they allow for easier movement of the ions through the electrolyte, facilitating faster charge transfer and improving the overall performance of the battery. The greater the separation of ion pairs, the more efficient the ionic conductivity, which can help reduce internal resistance and lower the overpotentials during operation. According to transition state theory, the formation of an activated complex as an unstable intermediate introduces kinetic hindrance to the charge transfer reaction, where the rate-determining step is often related to the dissociation of this activated complex. Therefore, the overpotential of the reaction may stem from ionic and mass transport limitations within the electrolyte. In fact, both hindered glymes exhibit a significantly sudden initial potential drop compared to G1 and G2, suggesting a greater energy requirement to initiate the process.[30] In this context, it is evident that the presence of *tert*-butyl groups contributes to the increase in overpotential, potentially due to steric effects that hinder the formation of the intermediate complex. This effect may be related to differences in the solvation behaviour of Na^+ cations.

The overpotential could be also associated with enhanced stabilization of discharge products in the electrolyte solution. Lutz *et al.* previously described this mechanism, known as solution-mediated.[29] It is primarily governed by the ability of solvents to stabilize Na^+ cations within the electrolyte through coordination interactions. Accordingly, solvents and additives with high Gutmann acceptor and donor numbers (AN and DN) are expected to promote the solution-mediated mechanism. Conversely, solvents with lower DN values exhibit a reduced ability to form ion pairs with intermediate oxygen species generated during discharge, thereby favouring the formation of sodium peroxide (Na_2O_2) rather than sodium superoxide (NaO_2) as the primary discharge product.[31] As previously mentioned, solvent chain length influences the predominant discharge mechanism, in agreement with prior studies.[11,29] Shorter-chain glymes facilitate the stabilization of discharge products in solution, while longer-chain glymes promote the precipitation of discharge products as a thin nanometric layer on the electrode surface, a process known as surface-mediated discharge.

In the case of H-G1, despite the presence of a bulkier terminal group, the solvent is able to stabilize a greater quantity of discharge products before blocking the electrode surface, in contrast to longer-chain solvents (G2 and H-G2).

However, the *tert*-butyl group reduces the overall discharge capacity of H-G1 compared to G1, likely due to weaker interactions between the Na^+ cations and the H-G1 solvent. For the longer-chain solvents (G2 and H-G2), a comparable trend is observed, with the non-hindered glyme exhibiting a lower overpotential than its hindered counterpart. To gain a deeper understanding of the influence of the *tert*-butyl substituent on glymes of varying chain lengths, a more comprehensive investigation into the stabilization (solvation) of electrolyte species, as well as their subsequent desolvation processes, is required. This will be further analysed in the following sections.

To investigate the effects of the lower conductivity of hinder glymes (Table 1) and the impact of the *tert*-butyl group under high-current conditions, a rate capability test using H-G1 was conducted (Fig. S1). The discharge overpotential is acceptable at 75 and 100 μA cm^{-2} but increases notably at 150 μA cm^{-2}. While low conductivity may influence overpotential, it does not significantly limit discharge capacity under high-rate conditions. In fact, the capacity at higher current densities is improved, particularly at 100 μA cm^{-2}. At lower current densities (75 μA cm^{-2}), NaO_2 may tend to form a compact film, likely passivating the electrode quickly and restricting electron flow. At higher current densities (100 μA cm^{-2}), more porous or dispersed particle formation occurs due to faster nucleation and less time for growth, reducing passivation and allowing for more NaO_2 accumulation. Additionally, at lower current densities, side or parasitic reactions (*e.g.*, Na_2O_2 formation or reactions with the electrolyte) may reduce effective capacity. Higher current densities can kinetically suppress these slower side reactions, favouring NaO_2 formation and capacity retention. At a current density of 150 μA cm^{-2}, the solvent's ability to solvate/desolvate becomes less dominant, while other physicochemical parameters such as viscosity and ionic conductivity play a more critical role. If viscosity is too high, it can severely limit diffusion, while ionic conductivity is essential for efficient charge transfer. However, these factors do not seem to prevent H-G1 from remaining competitive in terms of discharge capacity (Fig. 2) and rechargeability (Fig. 4) when compared to unhindered glymes. In fact, a deeper analysis of how other factors influence the performance of H-G1 at high currents is necessary and will be addressed in future studies.

In cyclability studies, it is not only crucial to understand how discharge products are formed but also to assess the ability of the system to electrochemically decompose them. It is important to note that the typical discharge products in Na–O_2 batteries are inherently insulating.[32] If the system is unable to fully reverse their formation during the charging process, these products will accumulate on the electrode surface over successive cycles, ultimately leading to premature battery failure. Fig. 3 presents the cycling tests for the different solvents under a cut-off capacity of 0.25 mAh cm^{-2} at 75 μA cm^{-2}, along with the evolution of overpotential throughout the cycles. Additionally, the galvanostatic profiles for selected cycles are shown in Fig. 4. Notably, the cycle life is significantly improved, with a doubling of performance simply by switching from G1 to G2. Both glymes exhibit high donor numbers (approximately 22 kcal mol^{-1}), indicating a certain ability to dissolve the

discharge products. For G2, the solvent exhibits an ideal trade-off between facilitating Na^+ solvation and desolvation while simultaneously stabilizing O_2^- through ion pair formation (chelating effect).[11] Additionally, its ability to dissolve discharge products, influenced by its donor number, contributes to enhanced cycling stability compared to G1. For hindered glymes, however, the monoglyme shows better cyclability than the diglyme (Fig. 3a). More importantly, the cycling

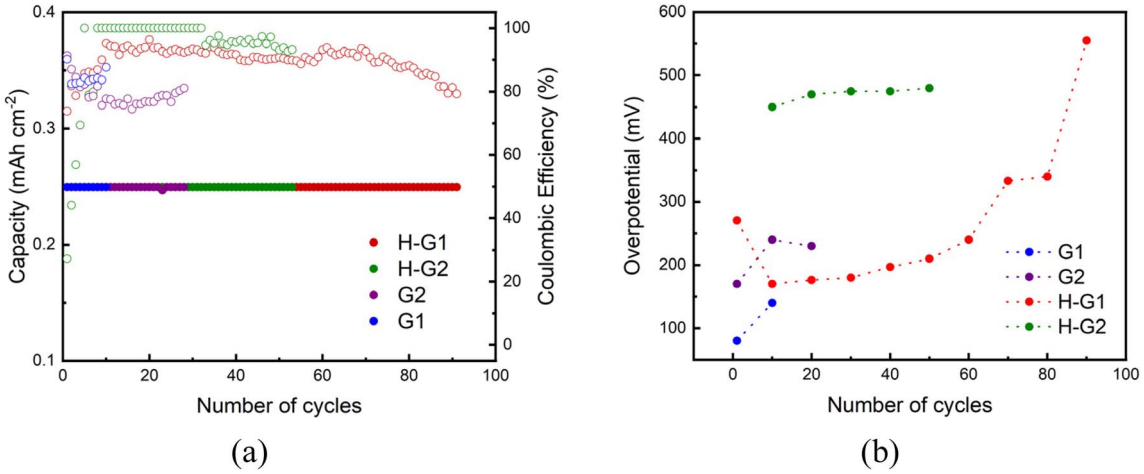

Fig. 3 (a) Cycling behaviour of Na–O_2 cells in different glymes to a fixed capacity (0.25 mAh cm^{-2}) at 75 μA cm^{-2}. Filled symbols represent discharge capacity values, while empty symbols correspond to coulombic efficiency. (b) Evolution of the overpotential throughout cycling for the different glymes.

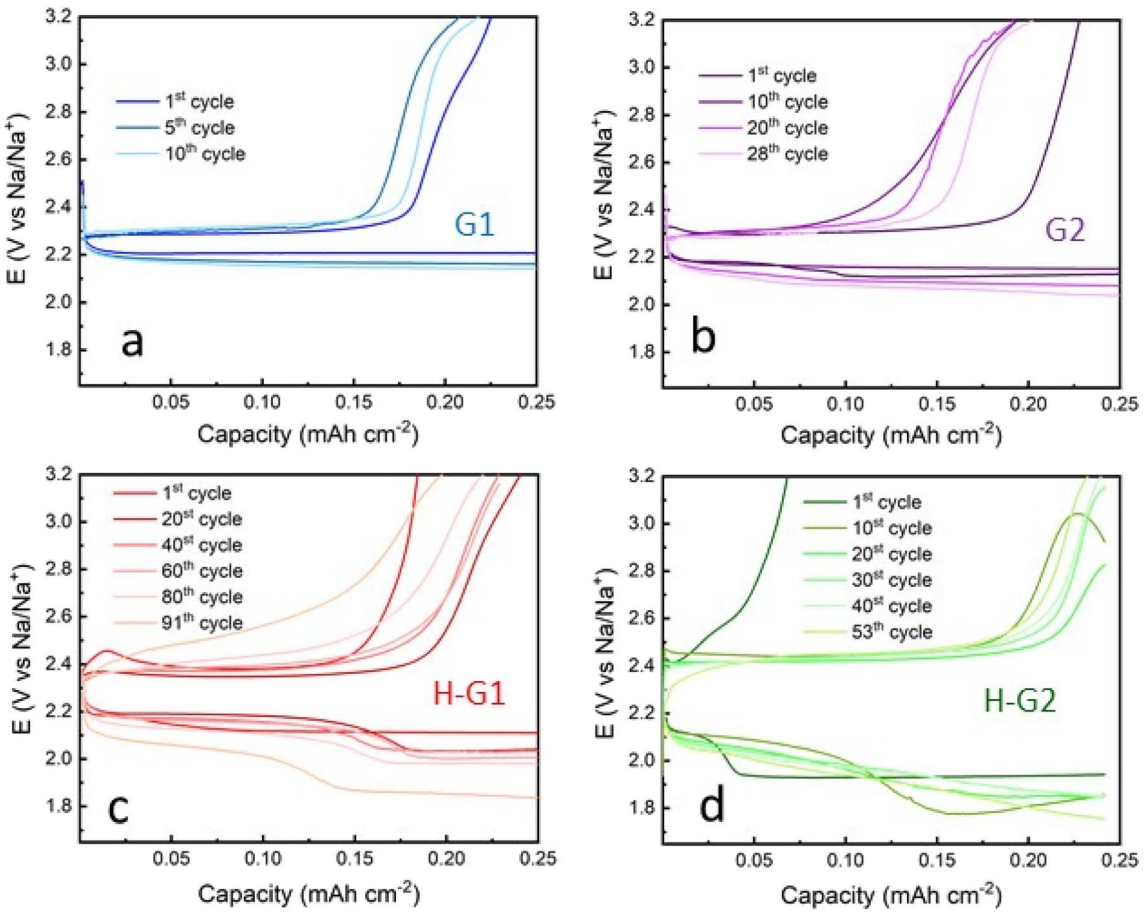

Fig. 4 Galvanostatic cycling of sodium–oxygen batteries at 75 μA cm^{-2} in 1 M NaTFSI at a capacity cut off 0.25 mAh cm^{-2} and (a) G1, (b) G2, (c) H-G1 and (d) H-G2 glymes in the electrolyte formulation.

performance of the batteries is significantly enhanced when hindered glymes are used in the electrolyte formulation. In the case of hindered monoglyme, the number of cycles without capacity fading increases from 10 to 91 due to the presence of the *tert*-butyl group in the ether structure. Regarding coulombic efficiency, the hindered glymes also outperform their conventional counterparts. The presence of *tert*-butyl groups likely influences the solvation and desolvation mechanisms, thereby affecting the overall electrochemical behaviour of the system.

The cycling overpotential (hysteresis) was evaluated at a capacity of 0.10 mAh cm^{-2}, showing a significant increase for H-G2 (450–470 mV), while remaining remarkably low for G1 (80–170 mV) (Fig. 3b and 4). G2 and H-G1 exhibit a moderate overpotential, with H-G1 displaying a slightly lower value (~170 mV *vs.* 230 mV) around cycle 20. By the end of the cycling, both solvents reach an overpotential of approximately 320 mV. The profiles of the curves throughout the galvanostatic cycling are qualitatively similar, as can be seen in Fig. 4. As previously mentioned, a greater difference between the discharge and charge potentials (overpotential) is observed for the hindered glymes.

The differences in voltage plateaus and cycling polarization can be attributed to several factors, among which the nature of discharge products – primarily NaO_2 and Na_2O_2 – is particularly significant.[33] While the solvents G1 and G2 exhibit a single reaction (plateau) at approximately 2.2 V *vs.* Na^+/Na, the hindered glymes display multiple processes. In the case of H-G1, an initial plateau is observed around 2.2 V *vs.* Na^+/Na, followed by a second distinguishable process occurring between 1.5 and 2.05 V *vs.* Na^+/Na. This second process gains prominence as cycling progresses, with a decreasing potential at which it occurs. A similar situation is observed for H-G2, although the plateaus are less clearly distinguishable.

The presence of multiple discharge processes suggests the formation of discharge products of different natures. Considering the thermodynamic standard potentials of various sodium oxides ($E\{Na_2O\} = 1.95$ V, $E\{NaO_2\} = 2.27$ V, and $E\{Na_2O_2\} = 2.33$ V),[1,34] the process occurring around 2.2 V *vs.* Na^+/Na probably results in NaO_2 as the primary discharge product. If a second reaction occurs at lower potential, it is reasonable to assume that the discharge product may further evolve into other compounds. Dilimon *et al.* reported a second reaction following NaO_2 formation at lower potential, attributed to the reduction of superoxide to peroxide, and a third reaction at even lower potential was assigned to the reduction of surface-adsorbed Na_2O_2 to Na_2O.[35] The formation of sodium peroxide from superoxide under specific conditions has also been reported by other authors.[36,37] Indeed, different studies have documented the formation of not only Na_2O_2 and NaO_2 as discharge products but also other species such as $Na_2O_2 \cdot 2H_2O$[10,38–40] and Na_2CO_3.[7,41,42]

The formation of hydrated sodium peroxide ($Na_2O_2 \cdot 2H_2O$) mostly is attributed to the decomposition of ether-based electrolytes, which release H_2O molecules due to the attack by the O_2^- species of the electrolyte.[43] This phenomenon was confirmed using tetraglyme (TEGDME, G4) as a solvent, demonstrating that this attack could extract protons from the solvent, which then react with O_2 to form H_2O.[44] The formation of discharge products such as $Na_2O_2 \cdot 2H_2O$ or Na_2CO_3 is generally undesirable, as they exhibit lower reversibility compared to NaO_2.[7,45,46] The evolution of NaO_2 discharge products towards $Na_2O_2 \cdot 2H_2O$ becomes more significant under flowing pure O_2 conditions.[43] The relationship between O_2 flow and the formation of hydrated sodium peroxide has also been linked to the potential presence of a very low amount of water in the O_2 stream.[47] Therefore, to prevent the formation of the hydrated compound, these cells are typically evaluated under static O_2 conditions, as performed in this study. For the solvents G1 and G2, electrochemical processes appear to predominantly yield NaO_2. However, the presence of *tert*-butyl groups seems to favour the formation of $Na_2O_2 \cdot 2H_2O$ as a secondary discharge product. As previously mentioned, the formation of secondary phases can be detrimental to the long-term cyclability of the battery, as they are not always completely reversed during charging. This accumulation can block the electrode surface and ultimately lead to premature system failure. However, while peroxide is more difficult to reverse than superoxide, it is not strictly considered a by-product. In fact, batteries using hindered glymes exhibit high reversibility, suggesting that peroxide formation does not pose a significant issue. In addition to the formation of different discharge products, variations in their morphology can also influence voltage and polarization. Consequently, the size, shape, and distribution of the discharge products can significantly impact the operating voltage and overall battery performance.

To determine the nature of the discharge products, a post-mortem characterization of the discharged and cycled cathodes was performed using Raman analysis, examining the chemical composition of the carbon cathode surface after full discharge (Fig. 2) and galvanostatic cycling (Fig. 5). After full discharge (Fig. 5a), G2 exhibited a well-defined and intense peak at 1156 cm^{-1}, corresponding to sodium superoxide (NaO_2). While this peak was also present in the other cathodes, additional phases were identified.[10] In the case of G1, sodium acetate (peaks at 753 and 336 cm^{-1}) was detected, whereas for the hindered glymes, hydrated sodium peroxide ($Na_2O_2 \cdot 2H_2O$), characterized by a shoulder at 1138 cm^{-1}, was observed. The formation of sodium acetate has been previously reported in the literature as a byproduct of electrolyte decomposition due to the attack by the highly reactive superoxide anion (O_2^-).[10,48] This reaction is attributed to the translocation of a hydrogen atom, facilitating the generation of a methyl-containing two-carbon unit of acetate.[48] It is worth noting that acetate, which is directly associated with the electrolyte decomposition, is only present in the spectra of the unhindered glymes and not in those of the hindered glymes, highlighting the enhanced stability of the latter. For the hindered glymes, the presence of hydrated sodium peroxide was significant, particularly in the case of H-G2, which correlates with the high cycling overpotential observed in Fig. 4. The formation of $Na_2O_2 \cdot 2H_2O$ is not solely due to solvent decomposition; other factors may contribute, so it should not be considered as a by-product like acetate.

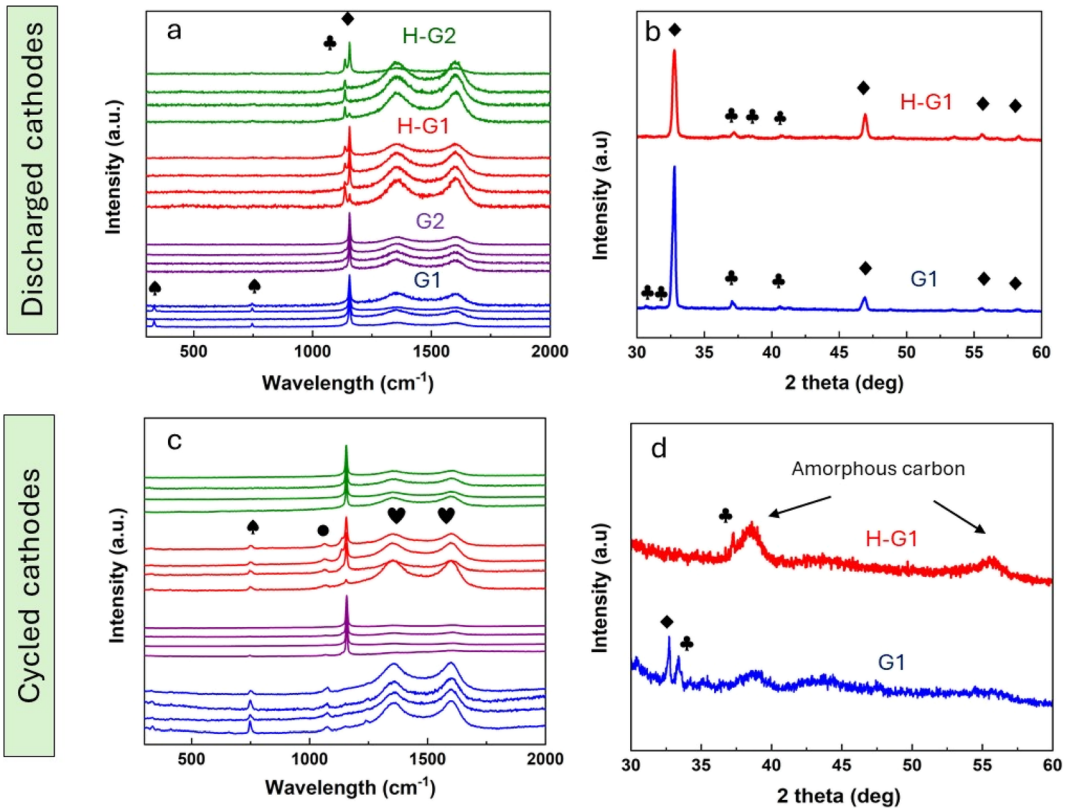

Fig. 5 (a and c) Raman mappings and (b and d) XRD patterns of the carbon paper cathodes after (a and b) full discharge and (c and d) cycling. The different phases identified by Raman spectroscopy[10] are presented by the following icons: ♥ carbon cathode, ◆ sodium superoxide (NaO_2), ♣ hydrated sodium peroxide ($Na_2O_2 \cdot 2H_2O$), ♠ sodium acetate (CH_3COONa) and ● sodium carbonate (Na_2CO_3).

To further investigate the discharge product chemistry, the electrodes discharged using G1 and H-G1 were analysed by XRD (Fig. 5b). It is important to note the limited airtightness of standard XRD sample holders, combined with the use of Kapton foil—employed to isolate air-sensitive samples while remaining transparent to X-rays—contributes to additional scattering. This increases baseline noise and reduces the peak-to-background ratio, making it particularly challenging to detect minor phases such as Na_2O_2, carbonates, or acetates, whose low-intensity peaks may become indistinguishable from the background. As a result, the combination of weak peak intensities and significant noise limits the reliability of phase identification by XRD. A 30-minute scan revealed a very similar diffraction pattern for both G1 and H-G1 after discharge. Both exhibit an intense peak at 32.6°, corresponding to the (200) reflection of NaO_2, along with a minor peak at 46.8°, corresponding to the (220) plane of NaO_2.[10] Additional minor peaks in the 28–31° range are associated with degradation products, mainly $Na_2O_2 \cdot H_2O$.[39] Consistently with Raman analysis, these results confirm that NaO_2 is the predominant discharge product in both electrolyte systems, along with some residual $Na_2O_2 \cdot 2H_2O$.

After cycling both G2 and H-G2 exhibit higher relative signal intensity corresponding to NaO_2 in Raman spectra (Fig. 5c), compared with their shorter chain counterparts (G1 and H-G1). This indicates that the charging performance of diglymes is inferior to that of monoglymes. The complete passivation of the cathode surface by the discharge product after cycling using diglymes as solvent suggests that the electrolyte is unable to redissolve these species during the oxidative charge. In the case of monoglymes, the NaO_2 peak disappears entirely for G1, while it remains faintly detectable for H-G1, where additional phases such as sodium acetate and carbonate are present as secondary products. The ability of H-G1 to redissolve the discharge products seems to be even more remarkable considering its cycling performance, which is nine times higher than G1. This enhanced performance of monoglymes in redissolving solid discharge products is confirmed by XRD analysis, where the intense peaks corresponding to superoxide phase completely disappeared in the cycled cathodes (Fig. 5d). Broad peaks, corresponding to amorphous carbon from the gas diffusion electrodes can be observed, together with very low intensity peaks corresponding to superoxide or peroxide species. Based on the cyclability test and post-mortem analysis, it can be concluded that the charging efficiency of hindered glymes, and particularly monoglyme, is significantly higher.

The morphology and distribution of discharge products on the oxygen electrode can provide valuable insights into their formation mechanism and the ability of the system to electrochemically reverse these products. For this reason, a scanning electron microscopy (SEM) analysis was conducted to examine the electrode surface after full discharge and at the end of

galvanostatic cycling, as shown in Fig. 6. The particle size of the discharge products after full discharge is significantly smaller for hindered glymes (2–4 μm) compared to conventional glymes (10–15 μm). This observation can be associated with a greater ability of G1 and G2 glymes to solubilize discharge products within the electrolyte, suggesting a solution-mediated mechanism. In the case of hindered glymes, the steric hindrance introduced by the *tert*-butyl groups may lead to weaker interactions of the type $[Na^{+}(glyme)_n\cdots O_2^{-}]$ in solvent-separated ion pairs. Additionally, monoglymes, both hindered and non-hindered, produce slightly smaller discharge product sizes. After cycling, the redissolution of NaO_2 cubes is much more evident in G1 and H-G1, where only a few isolated and small cubes are observed. In contrast, for G2 and H-G2, the surface appears to be blocked by a large number of cubic crystals, many of considerable size, with those in G2 being noticeably larger. These observations are fully consistent with the Raman analysis presented in Fig. 5c. However, for H-G1, passivation of the electrode surface with sodium salts or oxides is observed.

Based on the Raman and SEM analysis, the formation of a larger proportion of peroxide in hindered glymes could be attributed to two distinct phenomena (1) hindered glymes, similar to other glymes, are susceptible to nucleophilic attack by the superoxide anion, leading to hydrogen abstraction and the subsequent formation of H_2O, which in turn facilitates the formation of $Na_2O_2\cdot 2H_2O$,[44] or (2) differences in the morphology of the discharge products, driven by the nature of the electrolyte solvent. Hence, transmission X-ray microscopy studies have demonstrated that the surface layer of NaO_2 cubes is generally rich in decomposition products, surrounding an oxygen-deficient region that encloses the bulk of these cubes.[7] The smaller the cubes, the greater the surface area available for the deposition of secondary products.

To monitor the formation of water during cycling in G1 and H-G1 based cells, we conducted controlled experiments using two cells per electrolyte, each cycled to a limited capacity of 0.25 mAh cm^{-2} at a current density of 75 μA cm^{-2}. After 10 cycles, both the Celgard separator and GDL cathode were immersed in 1 mL of dry and fresh G1 to extract any water produced during the cycling process (Fig. S2a). The water content in 1 mL of fresh G1 and the solutions containing both the separator and the cathode were analysed by Karl-Fischer coulometric titrator (Fig. S2b). The measured water content values were very similar for both electrolyte systems, indicating that the observed differences in peroxide formation are not due to increased water generation in H-G1, but rather stem from the distinct morphology of the discharge products observed in Fig. 6.

The formation of $Na_2O_2\cdot 2H_2O$, attributed to the increased reactivity of the smaller NaO_2 discharge particles generated when using hindered glymes, was further confirmed by XRD analysis. For this purpose, the acquisition time for the samples shown in Fig. 5b was extended to 1 hour. This prolonged exposure resulted in a noticeable decrease in the intensity of the main NaO_2 peak at 32.6° for both G1 and H-G1 systems. In the case of H-G1, a clear degradation to $Na_2O_2\cdot 2H_2O$ after 1 hour was observed, confirming the high sensitivity of the small cubes discharged in the presence of hindered glymes (Fig. S3).

To gain further insight into the electrochemical processes occurring at the cathode–electrolyte interface, *in situ* monitoring of the first ten galvanostatic cycles was performed by complex impedance spectroscopy in three-electrode Na–O_2 cells employing either G1 or H-G1 as electrolyte solvent. The reference electrode consisted of a piece of sodium metal, while the working electrode was carbon paper, and a sodium metal foil served as counter electrode. The impedance response of each cell was recorded every two hours during the first discharge cycle and subsequently at the end of discharge and charge in each of the next nine cycles.

Fig. 7 presents the results of the fitted Nyquist plots at various stages of discharge and charge for both electrolyte systems. The experimental data were interpreted using the equivalent circuits shown in Fig. S4, which incorporate up to three distinct resistive contributions, depending on the state of the battery. The first, R_0, corresponds to the ohmic resistance of the cell, encompassing the current collectors, the contact interfaces, and even wiring effects. R_0 also includes the intrinsic

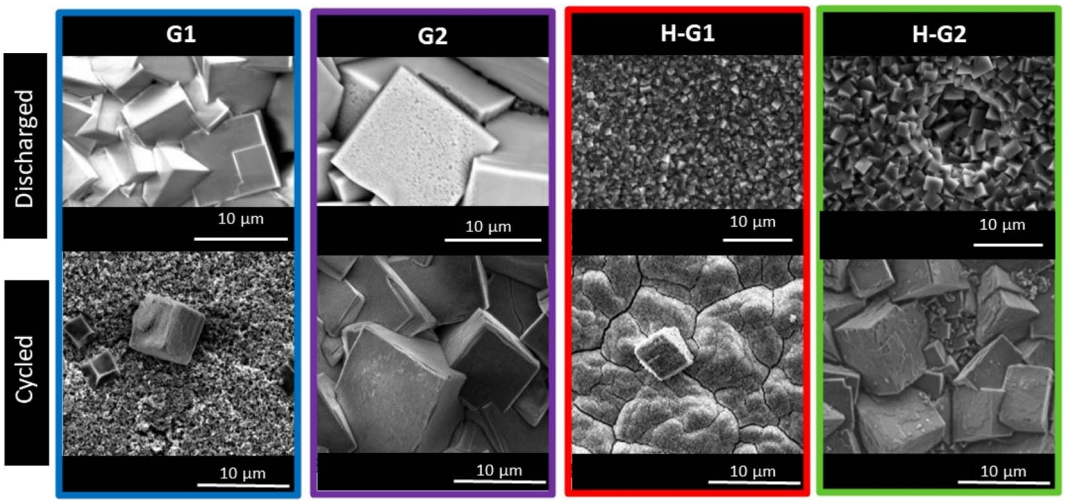

Fig. 6 SEM imaging of the carbon paper cathodes after full discharge and cycling.

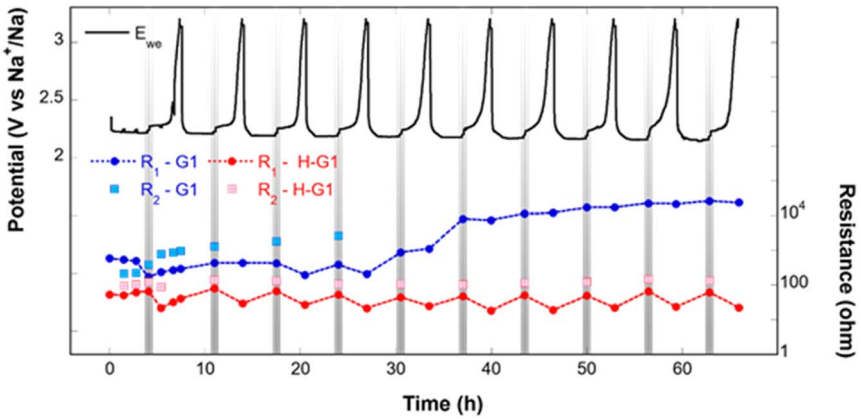

Fig. 7 Evolution of the fitted resistance values obtained from complex impedance spectroscopy measurements during the first 10 galvanostatic cycles for G1 and H-G1 electrolyte systems. Note: the resistance axis is presented on a logarithmic scale to enhance visibility of the variations across multiple orders of magnitude.

ionic resistance of the electrolyte, which appears largely unaffected by the change in glyme structure, as evidenced by the similar and nearly constant R_0 values observed for both G1 and H-G1 throughout cycling. A slight increase in R_0 over time is noted and attributed to general cell aging. The two additional resistive elements, R_1 and R_2, are each placed in parallel with constant phase elements (CPEs), exhibiting characteristic capacitance values on the order of 10^{-4} F and 10^{-6} F, respectively. Based on these capacitance magnitudes and their evolution during cycling, R_1 is assigned to processes related to oxygen adsorption, diffusion, and the electrochemical reduction/oxidation of oxygen species (*i.e.*, ORR during discharge and OER during charge) at the cathode.[6] In contrast, R_2 is associated with charge transfer resistance at the cathode/electrolyte interface, dominated by the formation and decomposition of solid discharge products such as NaO_2 and Na_2O_2.[6]

As illustrated in Fig. 7, R_2 is not required to fit the impedance spectra at the onset of discharge for either G1 or H-G1, indicating the absence of solid discharge products at this stage. As the discharge progresses, however, R_2 becomes necessary to achieve a good fit, reflecting the gradual formation and accumulation of electronically insulating solid-phase products on the cathode surface. R_2 increases steadily until the end of discharge. Meanwhile, R_1 remains relatively stable throughout the discharge process, consistent with a steady-state ORR mechanism once initial activation is achieved.

During charging, a marked difference emerges between the two electrolytes. In H-G1, R_2 is initially present but gradually vanishes as charging progresses, suggesting effective decomposition of the discharge products and recovery of the cathode surface. In contrast, R_2 persists throughout the charging process in the G1-based cell and remains nearly constant in magnitude, indicating incomplete or less efficient oxidation of the discharge species and a less dynamic interface. These observations underscore the enhanced reversibility and interfacial dynamics enabled by the H-G1 system.

The behavior of R_1 during the charging process is similar in both systems, showing a slightly increase toward the end of charge. This phenomenon has previously been attributed to electrode passivation and poor solid–solid contact between insulating discharge products and the conductive matrix.[49] Additionally, the accumulation of decomposition byproducts such as Na_2CO_3 has been shown to hinder charge transfer by physically blocking active sites,[7] resulting in a gradual increase of R_1 over extended cycling, as observed for G1 by Raman spectroscopy.

Notably, while the qualitative evolution of R_1 and R_2 follows similar trends in both electrolytes, their absolute values are consistently higher in the G1-based system. This difference becomes more pronounced after several cycles. Fig. S4 displays the fitted impedance spectra at the end of the first discharge and the end of the first charge for both electrolytes. For H-G1, the separation between R_1 and R_2 contributions is clearly distinguishable, and the disappearance of R_2 upon charging is evident. In the case of G1, however, the contributions of R_1 and R_2 become increasingly overlapped from the fourth cycle onward, making their individual deconvolution unreliable. Moreover, the progressive accumulation of non-reversible discharge products or parasitic byproducts in G1 leads to a substantial increase in total cell resistance, eventually causing premature cell failure.

Altogether, these findings demonstrate that under the present cycling conditions, the hindered monoglyme (H-G1) enables more efficient decomposition of discharge products and fosters the formation of a lower resistance cathode–electrolyte interface. This improved performance is attributed to the enhanced chemical stability and more favorable solvation environment provided by the bulky *tert*-butyl-terminated glyme structure.

The enhanced performances observed with hindered glymes prompted a more in-depth analysis using MD simulations to better understand the differences in the coordination environment of Na^+ across the four solvents. To achieve this, the radial distribution function (RDF) was computed to examine the interaction of Na^+ with the different molecular species in the electrolyte (Fig. 8). Specifically, the interactions with the oxygen atoms of the solvent molecules and $TFSI^-$ anions were analysed to assess the degree of dissociation of the NaTFSI salt in each

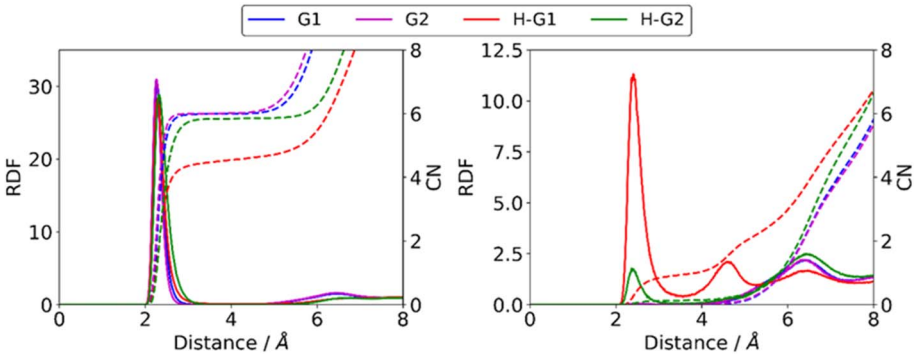

Fig. 8 Radial distribution functions (RDFs) of the Na^+–solvent (left) and Na^+–$TFSI^-$ (right) interactions (solid lines) along with the corresponding coordination numbers (dashed lines).

solvent. Both interactions were evaluated using the oxygen atoms of the observable molecules as coordination points for Na^+.

The RDF results indicate that Na^+ preferentially coordinates with solvent molecules rather than with $TFSI^-$. For both G1 and G2 systems, the Na^+–$TFSI^-$ interaction is negligible, as no coordination peak is observed in the RDF plots below 6 Å. However, a minor peak appears in H-G2, along with a low coordination number (CN), suggesting a weak but non-negligible interaction between Na^+ and $TFSI^-$. In contrast, H-G1 exhibits a significantly stronger Na^+–$TFSI^-$ interaction, as reflected by a CN of ~1, indicating that, on average, one oxygen atom from $TFSI^-$ is present in the coordination environment of Na^+. Regarding the Na^+–solvent interaction, G1, G2, and H-G2 display similar behaviour, with a CN of ~6 after the first RDF peak. However, for H-G1, despite a comparable RDF peak height, the CN decreases to ~4.5.

To further explore the possible coordination environments of H-G1 we conducted a multimolecular interaction analysis (Fig. 9), considering that RDFs alone do not distinguish whether different molecules interact with Na^+ simultaneously or separately, as they provide only averaged data. A cutoff of 3 Å is used to distinguish whether a molecule is part of the first coordination shell of Na^+. Therefore, Na^+ coordination was categorized into three scenarios: only solvent molecules, only $TFSI^-$ molecules, or a combination of both. Representative examples of the most probable coordination environments for each system were extracted from MD simulations for better visualization (Fig. 10).

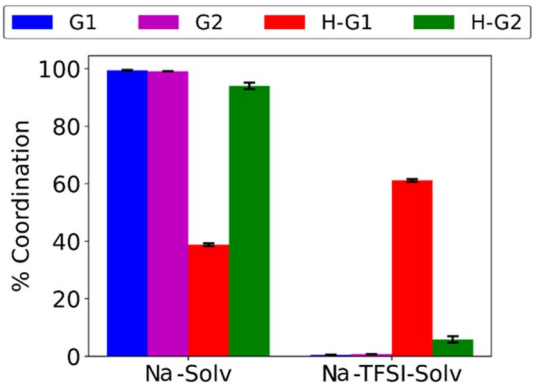

Fig. 9 Coordination environment of Na^+ in the different solvents, with error bars.

The analysis reveals that no isolated Na^+–$TFSI^-$ interactions are observed in any of the systems, confirming that the NaTFSI salt is at least partially solvated in the electrolyte. For G1 and G2, RDFs indicate almost negligible Na^+–$TFSI^-$ interactions, suggesting that nearly 100% of the coordination environment corresponds to Na^+–solvent interactions. Multimolecular interaction analysis confirms that only in less than 1% of cases, $TFSI^-$ enters the Na^+ coordination environment, likely due to random thermal vibrations that temporarily bring a $TFSI^-$ anion close to Na^+, which is quickly displaced by the more favourable solvent coordination. The RDF results further suggest that Na^+ preferentially coordinates with three G1 molecules (Fig. 10a) or two G2 molecules (Fig. 10b), maintaining a CN of approximately 6.

In the H-G2 system, the proportion of Na^+–TFSI–solvent coordination increases to 6%, implying that the presence of the *tert*-butyl group slightly reduces the ability of the solvent to fully solvate NaTFSI, allowing $TFSI^-$ to enter the Na^+ coordination environment. When Na^+ is coordinated exclusively with H-G2 (94% of cases), it is typically surrounded by two solvent molecules (Fig. 10e). However, when both H-G2 and $TFSI^-$ are present, two distinct configurations emerge: either two H-G2 molecules and one $TFSI^-$, or one H-G2 molecule and two $TFSI^-$, with a preference for the latter.

In the H-G1 system, the most common coordination environment for Na^+ involves a mixture of H-G1 and $TFSI^-$ molecules. In approximately 40% of cases, Na^+ is coordinated exclusively by H-G1, typically interacting with 3 solvent molecules (Fig. 10d). Coordination with only 2 H-G1 molecules also occurs, though less frequently, at an approximate ratio of 8 : 1 compared to the three-molecule configuration. This suggests that the bulky *tert*-butyl group in H-G1 impedes solvent–cation interactions, limiting closer packing. In the remaining 60% of cases, Na^+ is coordinated by a mixed environment of $TFSI^-$ and H-G1, with the most prevalent structure comprising two H-G1 molecules and one $TFSI^-$ (Fig. 10c). Other coordination configurations are observed only rarely.

Snapshots of the most probable configurations (Fig. 10) were generated using a cut-off distance of 3 Å to represent bonds between Na^+ and oxygen atoms. Notably, in the $1Na^+$–3H-G1

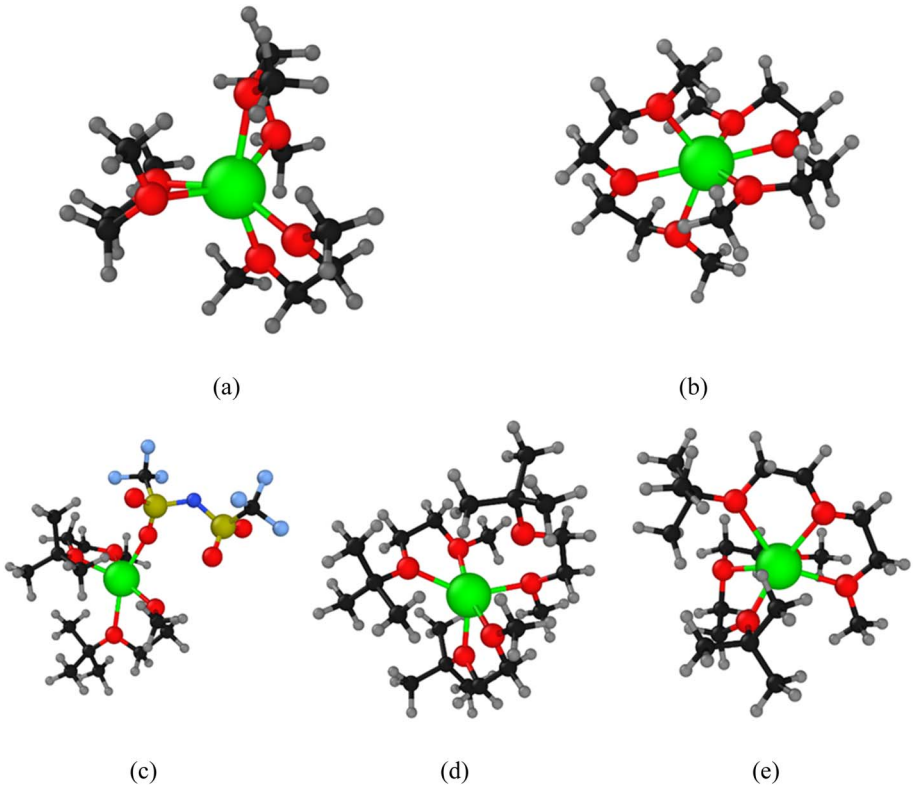

Fig. 10 Snapshots of the most probable configurations: (a) $1Na^+$–3G1, (b) $1Na^+$–2G2, (c) $1Na^+$–2H-G1–$1TFSI^-$, (d) $1Na^+$–3H-G1, and (e) $1Na^+$–2H-G2. Colour legend: Na – green; O – red; C – black; H – gray; S – yellow; N – dark blue; F – light blue.

configuration (Fig. 10d), one oxygen from an H-G1 molecule lies beyond the cut-off distance. This suggests that the introduction of the *tert*-butyl group reduces molecular flexibility, preventing the completion of the typical 6-oxygen coordination environment around Na^+.

To unveil the role of the different solvation structures between hindered and conventional glymes on the SEI composition, XPS analysis on the anodes recovered from cycled cells was carried out. Specifically, anodes subjected to 8 cycles with G1 and H-G1 were analyzed, since the highest difference in the solvent *vs.* salt coordination was found for the monoglymes (Fig. 10). Fig. 11 shows the most characteristic photoelectron peaks of the elements present in the analysed samples surface (F 1s, O 1s, C 1s and S 2p). Additionally, the surface elemental composition as calculated by integrating all main photoelectron peaks is also provided. From Fig. 11b, the higher inorganic character (richer in salt derived products) of the SEI formed with H-G1 is evidenced by the greater amount of F, S and N, together with a slightly decreased C content. A close look to the fittings of the provided photoelectron peaks in Fig. 11a reveals a larger contribution of inorganic $TFSI^-$ reduction products such as NaF, Na_2SO_3 or Na_2O in the H-G1 electrolyte.[12,50,51] Conversely, the anode that was cycled with G1 is richer in carbonates. Raman analysis of the discharge carbon cathodes in G1-based cells also revealed the presence of carbonates (Fig. 5), confirming a greater decomposition of the unhindered glyme compared to the hindered glyme. These findings can be attributed to differences in solvation shells, as the stronger Na^+–TSI^- coordination in H-G1 facilitates greater $TFSI^-$ anion access to the anode surface, promoting its reduction and leading to a more inorganic interphase. Salt-derived inorganic rich SEIs are typically more compact, ionically conductive and stable, which contributes to improved cyclability.[12,52,53]

A depth profile analysis of the SEI, assisted by 1 keV Ar^+ ion etching at varying accumulated sputter times, is provided in Fig. S5. The peaks corresponding to NaF, Na_2SO_3 and Na_2O inorganic species increase with etching time, while the carbonate peak barely changes, pointing towards higher inorganic content in the deeper SEI region in both cases. The fact that the peak around 531.7 eV (related to O in carbonates/hydroxides) increases slightly with etching time, while that at 289.6 eV (related to C in carbonates) remains unchanged, indicates that NaOH is also present in the SEI and located mainly at inner depths.[54]

A correlation can be established between the percentage of Na^+–$TFSI^-$ interactions (always occurring in the presence of solvent molecules) and the electrochemical performance observed in cycling tests. In the G1 and G2 systems, Na^+ is more effectively enclosed within the solvent structure, limiting its reactivity with other electrolyte components. Notably, G2 exhibits a stronger chelating effect than G1 due to the presence of three oxygen donor atoms capable of coordinating with Na^+. However, the longer molecular structure of G2 introduces steric hindrance, which restricts the ability of two G2 molecules to fully complete Na^+ solvation. Indeed, it has been demonstrated that the Na^+–G1 complex is more stable than the Na^+–G2

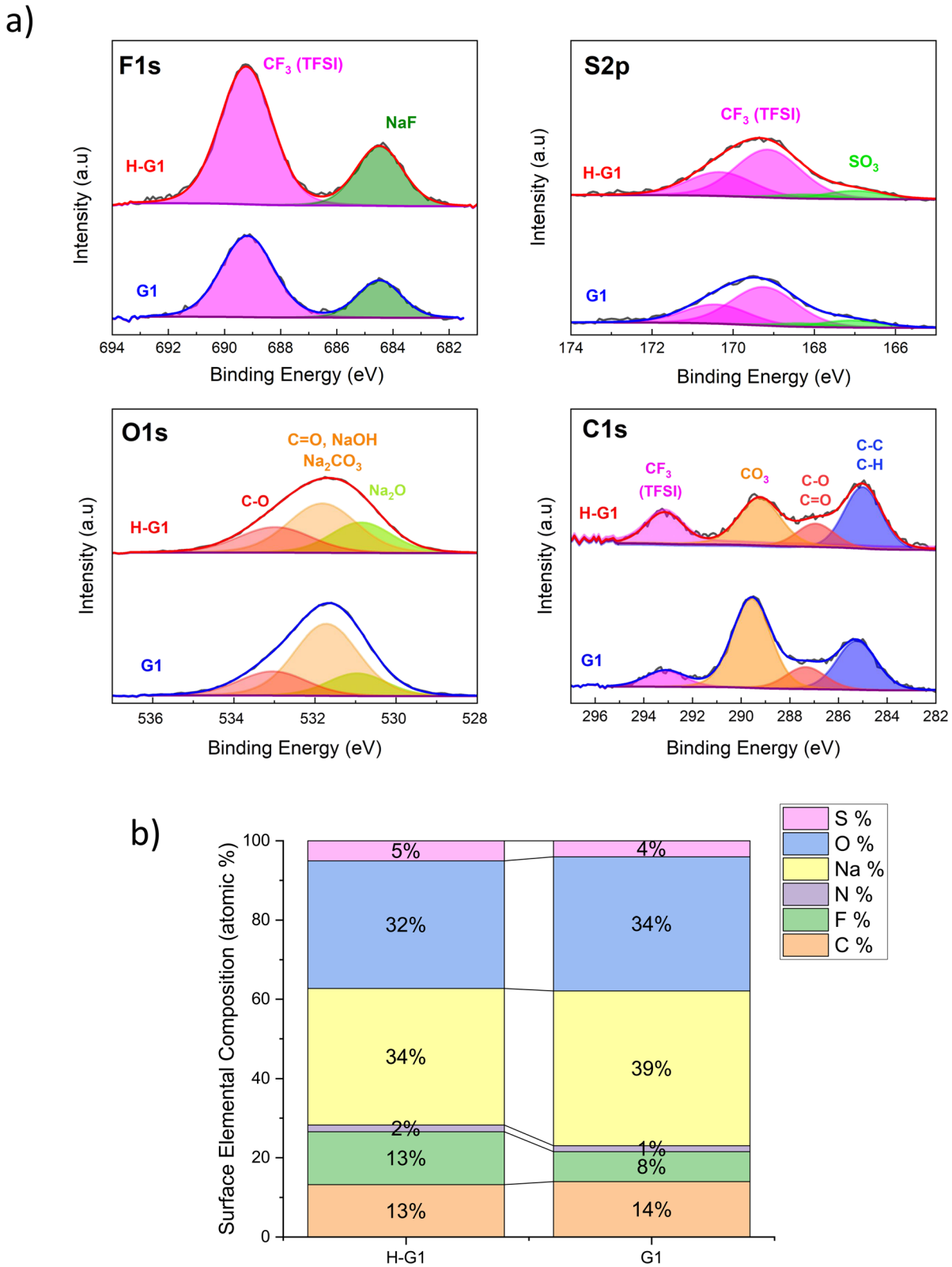

Fig. 11 (a) XP spectra in the regions of F 1s, S 2p, O 1s and C 1s for the anodes cycled with H-G1 and G1 electrolytes. (b) Surface elemental composition calculated from all integrated XPS peaks.

complex, leading to greater difficulty in desolvation in the case of G1.[11] Consequently, the cycling performance of G2 surpasses that of G1.

Conversely, in H-G1 and H-G2, the introduction of *tert*-butyl groups reduces solvent flexibility, impairing the ability to fully solvate Na^+. The bulky *tert*-butyl groups impose steric hindrance

and increase molecular rigidity, weakening Na^+–solvent interactions. This results in a diminished ability to stabilize discharge products in the electrolyte, leading to lower discharge capacity and smaller NaO_2 cubes in hindered glymes. On the other hand, the greater ease of Na^+ desolvation in H-G1 and H-G2 is associated with improved cycling performance. The steric hindrance imposed by *tert*-butyl groups is particularly pronounced in H-G1, where its shorter chain structure increases the probability of $TFSI^-$ entering the Na^+ coordination environment.

The role of the sodium salt counterion, $TFSI^-$ in this case, has been examined in previous studies, revealing that its chemical nature can influence Na^+ solvation.[55] This effect is particularly critical in weakly solvating solvents such as H-G1 (and to a lesser extent, HG2). While the incorporation of $TFSI^-$ into the Na^+ solvation shell does not critically affect the mechanism of discharge product formation, it promotes the formation of smaller discharge products, favoring $Na_2O_2 \cdot 2H_2O$ as a side product and increasing cycling overpotential. Importantly, this does not compromise cycle life and batteries using hindered glymes significantly outlast those with conventional glymes. The presence of $TFSI^-$ in the Na^+ coordination environment in H-G1 and H-G2 is correlated with changes in the chemical composition of the SEI.[53,55] The presence of $TFSI^-$ in the solvation shell leads to a more inorganic SEI, enriched with species such as NaF, Na_2SO_3, and Na_2O. Such inorganic-rich SEIs are associated with improved ionic conductivity and greater interfacial stability during cycling.[53,56,57] We therefore propose that the stronger Na^+–$TFSI^-$ interactions in H-G1 may contribute to the enhanced cycling stability observed in this system.

Conclusions

This study demonstrates the potential of hindered glymes as promising electrolyte solvents for sodium–oxygen ($Na–O_2$) batteries, offering an optimized balance between solvation capability and electrolyte stability. The inclusion of *tert*-butyl groups in the glyme structure introduces steric hindrance, which influences Na^+ solvation, desolvation, and discharge product stabilization. Our electrochemical analyses reveal that hindered monoglymes (H-G1) maintain high discharge capacities while significantly improving cycling stability, compared to conventional glymes. In contrast, hindered diglymes (H-G2) exhibit increased overpotentials due to steric limitations, but their electrochemical performance surpasses that of conventional diglymes (G2).

Molecular dynamics simulations provide deeper insights into the solvation environment, showing that hindered glymes exhibit weaker Na^+–solvent interactions, facilitating Na^+ desolvation. This is further confirmed by XPS and computational studies, which reveal that the weakened Na^+–solvent interaction promotes the inclusion of $TFSI^-$ in the solvation sphere of sodium, creating a more inorganic SEI that correlates to improved interfacial stability upon cycling. Post-mortem analysis confirms the formation of NaO_2 as the primary discharge product in most cases, while hindered glymes exhibit a higher proportion of secondary discharge products, such as $Na_2O_2 \cdot 2H_2O$, attributed to the smaller size of discharge products that increases their reactivity.

The extended cycle life observed for H-G1, compared to G1, can be attributed to differences in desolvation kinetics and SEI composition, driven by the distinct solvation structures of the two electrolytes. As discussed, the bulky *tert*-butyl groups in H-G1 disrupt the typical Na^+ solvation environment, weakening Na^+–solvent interactions, reducing overall solvation energy, and facilitating Na^+ desolvation. The coordination number (CN) analysis reveals a decrease from ~6 in G1 to ~5.5 in H-G1, indicating a more open coordination shell that supports easier desolvation.

These findings underscore the importance of solvent molecular design in tailoring electrolyte properties for $Na–O_2$ batteries. Hindered glymes emerge as a promising alternative to conventional glymes, offering enhanced thermal and health safety, improved cycle life, and a tuneable balance between discharge capacity and overpotential. Future research should focus on further optimizing molecular structures to mitigate side reactions and enhance electrolyte stability, thereby advancing the development of high-performance $Na–O_2$ batteries.

Conflicts of interest

There are no conflicts to declare.

Data availability

The data supporting the findings of this study, including electrochemical measurements, Raman spectra, scanning electron microscopy (SEM) images, and molecular dynamics simulation outputs, are included in the manuscript. Further data, if necessary, is available upon reasonable request.

Additional electrochemical and physicochemical characterization data. It contains discharge profiles at different current densities (Fig. S1), visual inspection and water content analysis of electrolytes after cycling (Fig. S2), XRD patterns of discharged electrodes with G1 and H-G1 solvents (Fig. S3), impedance spectra and fitted equivalent circuits (Fig. S4), and depth profile analyses of sodium anodes after cycling (Fig. S5). See DOI: **https://doi.org/10.1039/d5ta03233d**.

Acknowledgements

This work was supported by grant PID2023-151153OB-I00 funded by MICIU/AEI/10.13039/501100011033 and by FEDER, UE and by the Gobierno Vasco/Eusko Jaurlaritza under IT1546-22 project. The authors also acknowledge the financial support from the Basque Government through ELKARTEK Program under grant CICe2024, KK-2024/00062: "Profundizando en el conocimiento para el diseño y desarrollo de nuevos electrolitos y para tecnologias de baterías post-litio-ion". N. Ortiz-Vitoriano acknowledges grant RYC2020-030104-I funded by MICIU/AEI/10.13039/501100011033 and by ESF Investing in your future. The authors gratefully acknowledge Jorge Rebollar and

Mohamed Yahia for their invaluable assistance in laboratory operations.

References

1 I. Landa-Medrano, et al., Sodium-Oxygen Battery: Steps Toward Reality, *J. Phys. Chem. Lett.*, 2016, **7**, 1161–1166.
2 K. Song, D. A. Agyeman, M. Park, J. Yang and Y. M. Kang, High-Energy-Density Metal–Oxygen Batteries: Lithium–Oxygen Batteries vs Sodium–Oxygen Batteries, *Adv. Mater.*, 2017, **29**, 1–31.
3 C. Pozo-Gonzalo and N. Ortiz-Vitoriano, Recent progress, advances, and future prospects in Na–O_2 batteries, *Curr. Opin. Electrochem.*, 2022, **36**, 101120.
4 M. Yahia, I. R. de Larramendi and N. Ortiz-Vitoriano, Harnessing the Potential of (Quasi) Solid-State Na-Air/O_2 Batteries: Strategies and Future Directions for Next-Generation Energy Storage Solutions, *Adv. Energy Mater.*, 2024, 2401398.
5 I. Landa-Medrano, et al., New Insights into the Instability of Discharge Products in Na-O_2 Batteries, *ACS Appl. Mater. Interfaces*, 2016, **8**, 20120–20127.
6 I. Landa-Medrano, et al., Understanding the charge/discharge mechanisms and passivation reactions in Na-O_2 batteries, *J. Power Sources*, 2017, **345**, 237–246.
7 I. Landa-Medrano, et al., Architecture of Na-O_2 battery deposits revealed by transmission X-ray microscopy, *Nano Energy*, 2017, **37**, 224–231.
8 H. Yadegari and X. Sun, Sodium–Oxygen Batteries: Recent Developments and Remaining Challenges, *Trends Chem.*, 2020, **2**, 241–253.
9 D. Di Lecce, et al., Glyme-based electrolytes: Suitable solutions for next-generation lithium batteries, *Green Chem.*, 2022, **24**, 1021–1048.
10 M. Enterría, et al., Driving the sodium-oxygen battery chemistry towards the efficient formation of discharge products: The importance of sodium superoxide quantification, *J. Energy Chem.*, 2022, **68**, 709–720.
11 N. Ortiz Vitoriano, et al., Goldilocks and the three glymes: How Na^+ solvation controls Na–O_2 battery cycling, *Energy Storage Mater.*, 2020, **29**, 235–245.
12 N. Ortiz-Vitoriano, et al., Unlocking the role of electrolyte concentration for Na-O_2 batteries, *Energy Storage Mater.*, 2024, **70**, 103501.
13 D. Shanmukaraj, S. Grugeon, S. Laruelle and M. Armand, Hindered Glymes for Graphite-Compatible Electrolytes, *ChemSusChem*, 2015, **8**, 2691–2695.
14 S. Tang and H. Zhao, Glymes as versatile solvents for chemical reactions and processes: From the laboratory to industry, *RSC Adv.*, 2014, **4**, 11251–11287.
15 N. Charalampous, et al., New insights into the oxidative and cytogenotoxic effects of Tetraglyme on human peripheral blood cells, *Sci. Total Environ.*, 2024, **954**, 176484.
16 N. Ortiz-Vitoriano, et al., Highly Homogeneous Sodium Superoxide Growth in Na-O_2 Batteries Enabled by a Hybrid Electrolyte, *ACS Energy Lett.*, 2020, **5**, 903–909.
17 M. J. Abraham, et al., GROMACS: High performance molecular simulations through multi-level parallelism from laptops to supercomputers, *SoftwareX*, 2015, **1–2**, 19–25.
18 D. Van Der Spoel, et al., GROMACS: Fast, flexible, and free, *J. Comput. Chem.*, 2005, **26**, 1701–1718.
19 E. K. Watkins and W. L. Jorgensen, Perfluoroalkanes: Conformational Analysis and Liquid-State Properties from ab Initio and Monte Carlo Calculations, *J. Phys. Chem. A*, 2001, **105**, 4118–4125.
20 R. C. Rizzo and W. L. Jorgensen, OPLS All-Atom Model for Amines: Resolution of the Amine Hydration Problem, *J. Am. Chem. Soc.*, 1999, **121**, 4827–4836.
21 M. L. P. Price, D. Ostrovsky and W. L. Jorgensen, Gas-phase and liquid-state properties of esters, nitriles, and nitro compounds with the OPLS-AA force field, *J. Comput. Chem.*, 2001, **22**, 1340–1352.
22 W. L. Jorgensen, D. S. Maxwell and J. Tirado-Rives, Development and testing of the OPLS all-atom force field on conformational energetics and properties of organic liquids, *J. Am. Chem. Soc.*, 1996, **118**, 11225–11236.
23 G. A. Kaminski, R. A. Friesner, J. Tirado-Rives and W. L. Jorgensen, Evaluation and reparametrization of the OPLS-AA force field for proteins via comparison with accurate quantum chemical calculations on peptides, *J. Phys. Chem. B*, 2001, **105**, 6474–6487.
24 W. L. Jorgensen and N. A. McDonald, Development of an all-atom force field for heterocycles. Properties of liquid pyridine and diazenes, *J. Mol. Struct.: THEOCHEM*, 1998, **424**, 145–155.
25 V. Havu, V. Blum, P. Havu and M. Scheffler, Efficient O(N) integration for all-electron electronic structure calculation using numeric basis functions, *J. Comput. Phys.*, 2009, **228**, 8367–8379.
26 V. Blum, et al., Ab initio molecular simulations with numeric atom-centered orbitals, *Comput. Phys. Commun.*, 2009, **180**, 2175–2196.
27 C. Lee, W. Yang and R. G. Parr, Development of the Colle-Salvetti correlation-energy formula into a functional of the electron density, *Phys. Rev. B: Condens. Matter Mater. Phys.*, 1988, **37**, 785.
28 A. D. Becke, Density-functional thermochemistry. III. The role of exact exchange, *J. Chem. Phys.*, 1993, **98**, 5648–5652.
29 L. Lutz, et al., High capacity Na-O_2 batteries: Key parameters for solution-mediated discharge, *J. Phys. Chem. C*, 2016, **120**, 20068–20076.
30 L. Garcia-Quintana, et al., Unveiling the Impact of the Cations and Anions in Ionic Liquid/Glyme Hybrid Electrolytes for Na–O_2 Batteries, *ACS Appl. Mater. Interfaces*, 2022, **14**, 4022–4034.
31 I. M. Aldous and L. J. Hardwick, Solvent-Mediated Control of the Electrochemical Discharge Products of Non-Aqueous Sodium–Oxygen Electrochemistry, *Angew. Chem., Int. Ed.*, 2016, **55**, 8254–8257.
32 O. Arcelus, C. Li, T. Rojo and J. Carrasco, Electronic structure of sodium superoxide bulk, (100) surface, and clusters using

hybrid density functional: Relevance for Na-O_2 batteries, *J. Phys. Chem. Lett.*, 2015, **6**, 2027–2031.
33 S. Zhao, B. Qin, K. Y. Chan, C. Y. V. Li and F. Li, Recent Development of Aprotic Na–O_2 Batteries, *Batteries Supercaps*, 2019, **2**, 725–742.
34 P. Hartmann, et al., A rechargeable room-temperature sodium superoxide (NaO_2) battery, *Nat. Mater.*, 2012, **12**, 228–232.
35 V. S. Dilimon, et al., Superoxide stability for reversible Na-O_2 electrochemistry, *Sci. Rep.*, 2017, **7**, 1–10.
36 A. Azaribeni, et al., Enhancing Cycle Life in Superoxide-Based Na–O_2 Batteries by Reducing Interface Reactivity, *Adv. Energy Mater.*, 2025, 2404703.
37 Q. Sun, et al., Atomic Layer Deposited Non-Noble Metal Oxide Catalyst for Sodium–Air Batteries: Tuning the Morphologies and Compositions of Discharge Product, *Adv. Funct. Mater.*, 2017, **27**, 1606662.
38 J. Kim, et al., Dissolution and ionization of sodium superoxide in sodium–oxygen batteries, *Nat. Commun.*, 2016, **7**, 1–9.
39 N. Ortiz-Vitoriano, et al., Rate-Dependent Nucleation and Growth of NaO_2 in Na-O_2 Batteries, *J. Phys. Chem. Lett.*, 2015, **6**, 2636–2643.
40 H. Yadegari, et al., On rechargeability and reaction kinetics of sodium–air batteries, *Energy Environ. Sci.*, 2014, **7**, 3747–3757.
41 S. K. Das, S. Xu and L. A. Archer, Carbon dioxide assist for non-aqueous sodium–oxygen batteries, *Electrochem. Commun.*, 2013, **27**, 59–62.
42 B. Mao, et al., Operando Ambient Pressure X-ray Photoelectron Spectroscopy Studies of Sodium–Oxygen Redox Reactions, *Top. Catal.*, 2018, **61**, 2123–2128.
43 N. Zhao, C. Li and X. Guo, Long-life Na–O_2 batteries with high energy efficiency enabled by electrochemically splitting NaO_2 at a low overpotential, *Phys. Chem. Chem. Phys.*, 2014, **16**, 15646–15652.
44 J. Kim, H. D. Lim, H. Gwon and K. Kang, Sodium–oxygen batteries with alkyl-carbonate and ether based electrolytes, *Phys. Chem. Chem. Phys.*, 2013, **15**, 3623–3629.
45 S. Y. Sayed, et al., Revealing instability and irreversibility in nonaqueous sodium–O_2 battery chemistry, *Chem. Commun.*, 2016, **52**, 9691–9694.
46 W. J. Kwak, L. Luo, H. G. Jung, C. Wang and Y. K. Sun, Revealing the Reaction Mechanism of Na-O_2 Batteries using Environmental Transmission Electron Microscopy, *ACS Energy Lett.*, 2018, **3**, 393–399.
47 C. Liu, et al., On the Stability of NaO_2 in Na-O_2 Batteries, *ACS Appl. Mater. Interfaces*, 2018, **10**, 13534–13541.
48 R. Black, et al., The Nature and Impact of Side Reactions in Glyme-based Sodium–Oxygen Batteries, *ChemSusChem*, 2016, **9**, 1795–1803.
49 D. Ma, J. Chen, F. Yu and Y. Chen, Probing the Origin of Overpotential for Sodium-Oxygen Batteries with Distribution of Relaxation Time, *Batteries Supercaps*, 2024, **7**, e202400257.
50 M. Armand, et al., Poly(vinyl butyrate) Esters as Stable Polymer Matrix for Solid-State Li-Metal Batteries, *ACS Energy Lett.*, 2025, **10**, 579–587.
51 P. Ranque, et al., Feasibility of Multifunctional Cellulose-Based Polysalt as a Polymer Matrix for Li Metal Polymer Batteries, *ACS Appl. Mater. Interfaces*, 2023, **15**, 51089–51099.
52 B. Acebedo, et al., On the role of ultrathin lithium metal anodes produced by thermal evaporation, *J. Power Sources*, 2024, **618**, 235218.
53 I. R. de Larramendi, et al., Unveiling the Role of Tetrabutylammonium and Cesium Bulky Cations in Enhancing Na-O_2 Battery Performance, *Adv. Energy Mater.*, 2022, **12**(2), 2102834.
54 L. Fallarino, et al., On the practical applicability of thermal evaporation technique to fabricate Na thin metal anodes for Na-metal batteries, *J. Power Sources Adv.*, 2024, **26**, 100137.
55 L. Lutz, et al., Role of Electrolyte Anions in the Na–O_2 Battery: Implications for NaO_2 Solvation and the Stability of the Sodium Solid Electrolyte Interphase in Glyme Ethers, *Chem. Mater.*, 2017, **29**, 6066–6075.
56 P. Stigliano, et al., Physicochemical properties of Pyr_{13}TFSI-NaTFSI electrolyte for sodium batteries, *Electrochim. Acta*, 2022, **412**, 140123.
57 H. Wu, et al., A Uniform Solid Electrolyte Interface Enabling Long Cycling in Sodium-Metal Batteries with Fast Charging, *ACS Appl. Mater. Interfaces*, 2025, **17**(12), 18286–18295.

